

See discussions, stats, and author profiles for this publication at: <https://www.researchgate.net/publication/232237937>

Autocatalytic reduction of a Cu₂O/Cu(111) surface by CO: STM, XPS, and DFT studies

ARTICLE *in* THE JOURNAL OF PHYSICAL CHEMISTRY C · OCTOBER 2010

Impact Factor: 4.77 · DOI: 10.1021/jp1029079

CITATIONS

24

READS

111

5 AUTHORS, INCLUDING:



Fan Yang

Chinese Academy of Sciences

33 PUBLICATIONS 691 CITATIONS

[SEE PROFILE](#)



Ping Liu

Brookhaven National Laboratory

118 PUBLICATIONS 4,182 CITATIONS

[SEE PROFILE](#)



Jan Hrbek

Brookhaven National Laboratory

213 PUBLICATIONS 6,010 CITATIONS

[SEE PROFILE](#)

Autocatalytic Reduction of a Cu₂O/Cu(111) Surface by CO: STM, XPS, and DFT Studies[†]

Fan Yang, YongMan Choi, Ping Liu, Jan Hrbek, and José A. Rodriguez*

Chemistry Department, Brookhaven National Laboratory, Upton, New York 11973

Received: March 31, 2010; Revised Manuscript Received: June 8, 2010

The reduction of a Cu₂O surface layer on Cu(111) by CO was studied using scanning tunneling microscopy (STM), X-ray photoelectron spectroscopy (XPS) and calculations based on density functional theory. Real-time XPS measurements show the existence of an induction time and an autocatalytic reaction for the reduction of the Cu₂O/Cu(111) surfaces. The reduction of the Cu₂O surface layer goes through two stages, the “slow reaction” regime and the “fast reaction” regime. During the “slow reaction” regime, an “O-deficient Cu₂O” phase forms and propagates on the surface, which lowers the reaction barrier for the removal of lattice oxygen in Cu₂O. The propagation of the “O-deficient Cu₂O” phase across the surface leads to the “fast reaction” regime, through which the reduction rate is approximately constant due to a “step-only” reaction mechanism. STM studies provide an atomic level picture for the intermediate structures and the reaction pathway during the reduction of the Cu₂O surface oxide. Upon the loss of chemisorbed oxygen from the typical Cu₂O honeycomb structure, a reconstruction occurs, and Cu₂O heptagons are formed. The “O-deficient Cu₂O” phase is a disordered phase linked to the formation of Cu₂O heptagons. The Cu₂O heptagons provide adsorption sites for CO, which reacts with chemisorbed oxygen hopped from neighboring Cu₂O honeycombs.

Introduction

The reduction of Cu₂O by carbon monoxide is critical to a number of applications in catalysis and material science. For many years, CuO_x-based catalysts have been used for reactions that involve the conversion of carbon monoxide, such as CO oxidation (2CO + O₂ → CO₂),^{1–3} alcohol synthesis (CO + 2H₂ → CH₃OH),⁴ and the water–gas shift reaction (CO + H₂O → CO₂ + H₂).⁵ CuO, Cu₄O₃, and Cu₂O are well-known copper oxides with monoclinic, tetragonal and cubic crystal structures, respectively.^{6–9} Thus, different intermediates can be present in the reduction process.^{5,9} In principle, the three possible pathways for the transformation of CuO to Cu by reaction with a reducing agent (CO, H₂, ethanol, etc) include a direct reduction (CuO → Cu, pathway 1) or reduction mechanisms that involve either one intermediate (CuO → Cu₂O → Cu, pathway 2) or two intermediates (CuO → Cu₄O₃ → Cu₂O → Cu, pathway 3).

Temperature-programmed reduction (TPR), synchrotron-based time-resolved X-ray diffraction, time-resolved extended X-ray absorption fine-structure, and X-ray absorption near-edge structure (XANES) were employed to study in a systematic way the reaction of powders of CuO and Cu₂O with CO or H₂ gas molecules.¹⁰ Both TPR and isothermal reduction results showed that CuO was easier to reduce than Cu₂O under the same reaction conditions. In situ measurements of XRD and XANES showed a direct transformation pathway for CuO reduction (CuO → Cu) when there was a large supply of CO, and a sequential step pathway involving one intermediate (CuO → Cu₂O → Cu) was seen with a limited supply of CO.^{10a} An induction period was seen for CuO or Cu₂O reduction in the presence of CO or H₂, and it was longer with decreasing temperature.¹⁰ A similar phenomenon was seen during the reduction of NiO, and the induction period reflected the need to have O vacancies and defects in the oxide surface to facilitate the adsorption of the reducing agent.⁹ O vacancies in CuO or Cu₂O could be formed

during the induction period that could foster the formation of nonstoichiometric metastable copper-oxide species. A Cu₂O-like intermediate showed extra disordered oxygen in the empty tetrahedral sites of Cu₂O.¹⁰ On the basis of these observations, there is a clear need to study at a microscopic level the interaction of CO with the surface of Cu₂O and CuO_{1-x}. The structural nature of key surface oxygen species remains to be described. Furthermore, an understanding of the intermediate structures formed during the reduction of surfaces of copper oxide is important for the catalytic processes mentioned above.

Recently, surface oxides of late transition metals have generated tremendous interest in fundamental studies of heterogeneous catalysis.^{11–19} Studies on the structural transitions in the surface of metal oxides during CO oxidation can facilitate our understanding of the surface reactivity of metal oxides.^{11b,20–22} In addition, many studies of CO titration have been conducted on a number of metal surfaces covered with chemisorbed oxygen.^{23–29} These studies demonstrated the utility of scanning tunneling microscopy (STM) as an excellent tool for identifying the reaction sites and for measuring the surface reaction kinetics at the atomic level. In this article, we combine STM, X-ray photoelectron spectroscopy (XPS), and calculations based on density functional theory (DFT) to obtain an atomic level picture of the reduction kinetics of a Cu₂O surface layer supported on Cu(111). We show how the formation of an intermediate phase leads to an autocatalytic reduction of the Cu₂O surface.

Experimental and Computational Methods

I. Experimental Studies. XPS and STM experiments were carried out in two separate chambers. XPS studies were conducted in a home-built chamber with a base pressure of 4 × 10⁻¹⁰ Torr. The chamber is equipped with a hemispherical electron energy analyzer, a quadrupole mass spectrometer, and a twin anode (Mg and Al) X-ray source. The O1s core levels were excited by Al K α radiation (1486.6 eV). The Cu(111) single crystal was held by two Ta legs of the manipulator and heated by applying current through the sample. The sample

[†] Part of the “D. Wayne Goodman Festschrift”.

* Corresponding author. E-mail: rodriguez@bnl.gov.

temperature was monitored by a type C thermocouple fixed in a hole of Cu(111).

STM studies were conducted in a commercial Omicron variable temperature STM system equipped with LEED, AES, surface cleaning facilities, and e-beam metal evaporator. The base pressure of the STM chamber was $<1 \times 10^{-10}$ Torr. The sample temperature was measured by a K-type thermocouple, which was installed on a linear motion feedthrough and pressed against the top of the sample surface. A resistive heater posited at the back of the sample could increase the sample temperature up to 1000 K. Chemically etched W tips were used for imaging the surface. The SPIP software (Image Metrology, Denmark) was used to process and analyze STM images. In our image processing, only routines such as slope correction and low pass filtering were applied.

The Cu(111) single crystal was pretreated in a mixed H₂/Ar flow at 500 °C to remove any possible sulfur impurities from the bulk. After being transferred into UHV, the sample was cleaned by repeated cycles of Ar sputtering (1 keV, 40 min) and annealing (900 K, 10 min). CO gas was cleaned using a trap of liquid N₂ prior to the reduction of the Cu₂O surface.

II. Density Functional Theory Calculations. We performed plane wave DFT calculations using the Vienna ab initio simulation package^{30,31} with projector augmented wave potentials.³² The generalized gradient approximation using the Perdew–Wang (PW91) exchange-correlation functional³³ was applied. All calculations were carried out with a 400 eV kinetic energy cutoff for a plane wave basis set and a Monkhorst–Pack³⁴ mesh with (3 × 3 × 3) and (3 × 3 × 1) k-points for bulk and surface calculations, respectively. The predicted lattice constant of Cu is 3.634 Å, which is in good agreement with an experimental value of 3.62 Å.³⁵ The flat Cu(111) surface was simulated by a three-layer 4 × 4 slab model, and one monolayer of Cu₂O was adsorbed on Cu(111) to model Cu₂O/Cu(111). The bottom two layers of the Cu surface were fixed at the lattice position, and the other atoms were allowed to fully relax during the optimization. To examine the difference with and without chemisorbed oxygen species at 3-fold hollow (fcc and hcp) sites on Cu₂O/Cu(111), similar to our previous study,³⁶ we calculated the electron localization function (ELF)^{37,38} on the basis of each optimized geometry. The charge transfer between the Cu₂O-like surface oxide and Cu(111) was calculated using the Bader analysis program,³⁹ based on Bader’s theory.^{40,41} The reaction energy (ΔE_R) of the CO titration, Cu₂O/Cu(111) + CO → Cu₂O_x/Cu(111) + CO₂, was computed, where Cu₂O/Cu(111) is a Cu₂O-like surface oxide formed on Cu(111) and Cu₂O_x/Cu(111) represents the product after removing one oxygen atom from the surface oxide or Cu(111). ΔE_R is expressed as follows:

$$\Delta E_R = \{E[\text{Cu}_2\text{O}_x/\text{Cu}(111)] + E[\text{CO}_2]\} - \{E[\text{Cu}_2\text{O}/\text{Cu}(111)] + E[\text{CO}]\} \quad (1)$$

The zero-point energy correction was also included according to the vibrational frequencies of the topmost layer of the Cu(111) surface and surface species (i.e., the oxide surface and chemisorbed oxygen species). Then the Gibbs free energies⁴² for the CO titration reaction were estimated at $T = 800$ K according to $\Delta G_R \approx \Delta E_R - T\Delta S$, where the entropies, S , for CO and CO₂ were determined according to ref 42.

Results and Discussion

I. The Reduction Kinetics of the Cu₂O/Cu(111) Surface.

A well-ordered Cu₂O surface was prepared by exposing the Cu(111) surface to 5×10^{-7} Torr O₂ at 650 K for 20 min, as

shown in Figure 1. Figure 1b displays the structure of the Cu₂O surface layer, which has unit cell vectors of 2.20 and 1.18 nm. The structure of this Cu₂O surface layer is often referred to as the “44” structure in previous studies on the oxidation of Cu(111),^{43–45} since the unit cell of the surface oxide is 44 times larger than the (1 × 1) unit cell of Cu(111). A structural model for this Cu₂O/Cu(111) system has been proposed by Jensen et al.^{44,45} and Matsumoto et al.⁴³ Both suggest the “44” structure originates from a distorted Cu₂O(111)-like layer grown epitaxially on Cu(111). The structure of the Cu₂O(111)-like layer is depicted in Figure 1c and compared with the structure of the (1 × 1)-Cu₂O(111) surface in Figure 1d. The Cu₂O(111)-like layer has the same honeycomb structure as that of the (1 × 1)-Cu₂O(111) surface, but with coordinatively under-saturated Cu atoms (cus-Cu) removed.^{43–46} XPS was also used to monitor the oxidation of Cu(111). After annealing the Cu(111) surface in 5×10^{-7} Torr O₂ at 650 K for 20 min, the O 1s XPS intensity reached a maximum value and stopped increasing upon further annealing in O₂. The trend of saturation in surface oxygen coverage is consistent with previous AES studies^{45,47} on the oxidation of Cu(111).

The reduction of the Cu₂O surface layer was conducted in the presence of CO, which reacts with surface oxygen and forms CO₂ to leave the surface at above 600 K. The reduction kinetics was measured by monitoring the XPS O 1s intensity in the presence of 6×10^{-8} Torr CO at 800 K (Figure 2). Prior to the CO exposure, the Cu₂O surface oxide was kept at 800 K for 1 h with no visible changes in the O 1s intensity, as monitored by XPS. A constant O 1s intensity rules out the possibilities of thermal/beam-induced oxygen desorption. In addition, since CO does not stick to the Cu or Cu₂O surfaces at 800 K, the measured changes in XPS O 1s intensity over time give the removal rates of oxygen from the Cu₂O surface oxide.

Previous studies for the reaction of CO with Cu₂O powders have shown the existence of an induction time before the reduction process starts.¹⁰ In Figure 2, the removal of surface oxygen can be divided into two stages, “slow reaction” and “fast reaction”. The “slow reaction” regime refers to the initial 2000 s of CO exposure, where the removal of surface oxygen remains negligible for ~1200 s, and then starts and accelerates to reach a fast reaction rate at ~2000 s. The “fast reaction” regime refers to the stage starting from ~2000 s of CO exposure until the complete reduction of Cu₂O surface layer, where the removal of surface oxygen remains at a fast and approximately constant reaction rate.

To obtain an atomic understanding of the reduction kinetics, STM snapshots were taken throughout the reduction of the Cu₂O/Cu(111) system. The total time for complete reduction, as measured in the STM chamber, is shifted from the time measured in the XPS chamber due to a difference in the pressure and temperature measurements of the two chambers. We adjusted the time measured in the STM study to the time measured in the XPS study. Figure 3a illustrates the morphology of Cu₂O surface layer after ~1000 s of CO exposure at 800 K. At the onset of surface reduction, the ordered large terrace of Cu₂O surface oxide is broken into smaller domains, with the boundaries decorated by bright dots. The structure of small domains is magnified in Figure 3b. Although the “44” structure is maintained within each small domain, surface areas surrounding the bright dots (domain boundary region) have lost their “44” structure and appeared as honeycomb arrays.

The relaxation from the strain-induced “44” structure to the honeycomb structure becomes more evident as the reduction reaction proceeds. After ~2000 s of CO exposure, the ordered

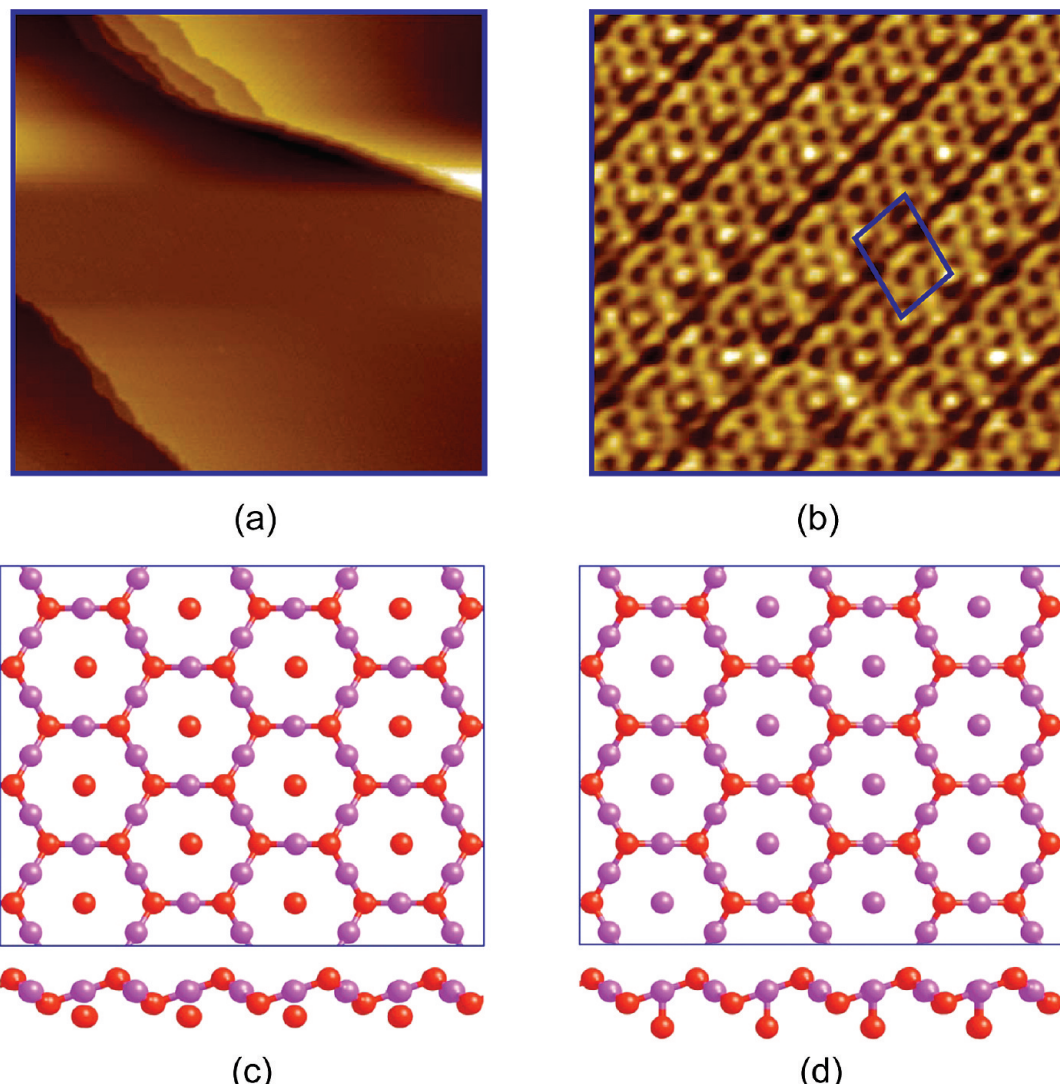


Figure 1. (a–b) STM images of the “44” structure of Cu_2O surface oxide, prepared by exposing $\text{Cu}(111)$ to 5×10^{-7} Torr O_2 at 650 K for 20 min. Image sizes are (a) $100 \times 100 \text{ nm}^2$ and (b) $10 \times 10 \text{ nm}^2$. (c–d) The structural models of a $\text{Cu}_2\text{O}(111)$ -like layer (c) and a $(1 \times 1)\text{-}\text{Cu}_2\text{O}(111)$ layer (d). Cu atoms are represented by purple balls, and O atoms are represented by red balls.

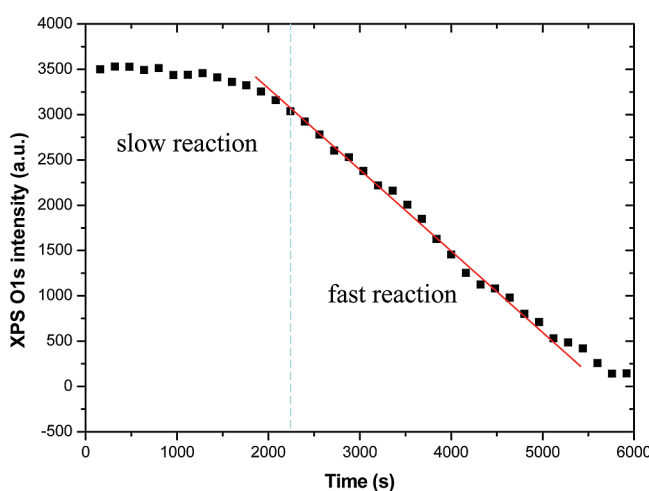


Figure 2. The reduction of the “44” Cu_2O surface oxide in 6×10^{-8} Torr CO measured by real-time XPS at 800 K. The dashed line shows the breakdown between the two reaction stages, “slow reaction” and “fast reaction”. The straight line is drawn to guide the eye.

domains of Cu_2O are replaced with bright dots distributed all over the surface (Figure 3c). Figure 3d shows a zoomed-in image

of the surface in Figure 3c. It is clear that the Cu_2O surface oxide has transformed into a honeycomb layer covered by bright dots. Noticeable in Figure 3c are a few dot-free surface areas, $\sim 10 \text{ nm}$ in width and marked by dashed lines. The structure of these areas is magnified in Figure 3e, which has a structure identical to the honeycombs observed in Figure 3b and 3d. The periodicity of these honeycomb structures is measured to be 0.60 nm , corresponding to the lattice spacing of the $\text{Cu}_2\text{O}(111)$ -like layer on $\text{Cu}(111)$.^{45,46,48}

The structural model of the $\text{Cu}_2\text{O}(111)$ -like layer on $\text{Cu}(111)$ is presented in Figure 3f, with two types of oxygen species; namely, chemisorbed oxygen and lattice oxygen within Cu_2O . Because the center of bright dots is aligned with the center of honeycomb arrays, the creation of a bright dot suggests the removal of a chemisorbed oxygen atom from the center of a Cu_2O honeycomb, forming an oxygen vacancy in the $\text{Cu}_2\text{O}(111)$ -like layer. The strain between the Cu_2O surface oxide and the Cu substrate is thus relaxed at the vacancy site locally, causing surface areas within a few nm of the vacancy site to transform from the “44” structure back to the honeycomb structure. As oxygen vacancies propagate across the surface, the “44” structure is completely removed and replaced with a defective $\text{Cu}_2\text{O}(111)$ -like layer, which we term as the “O-deficient Cu_2O ”

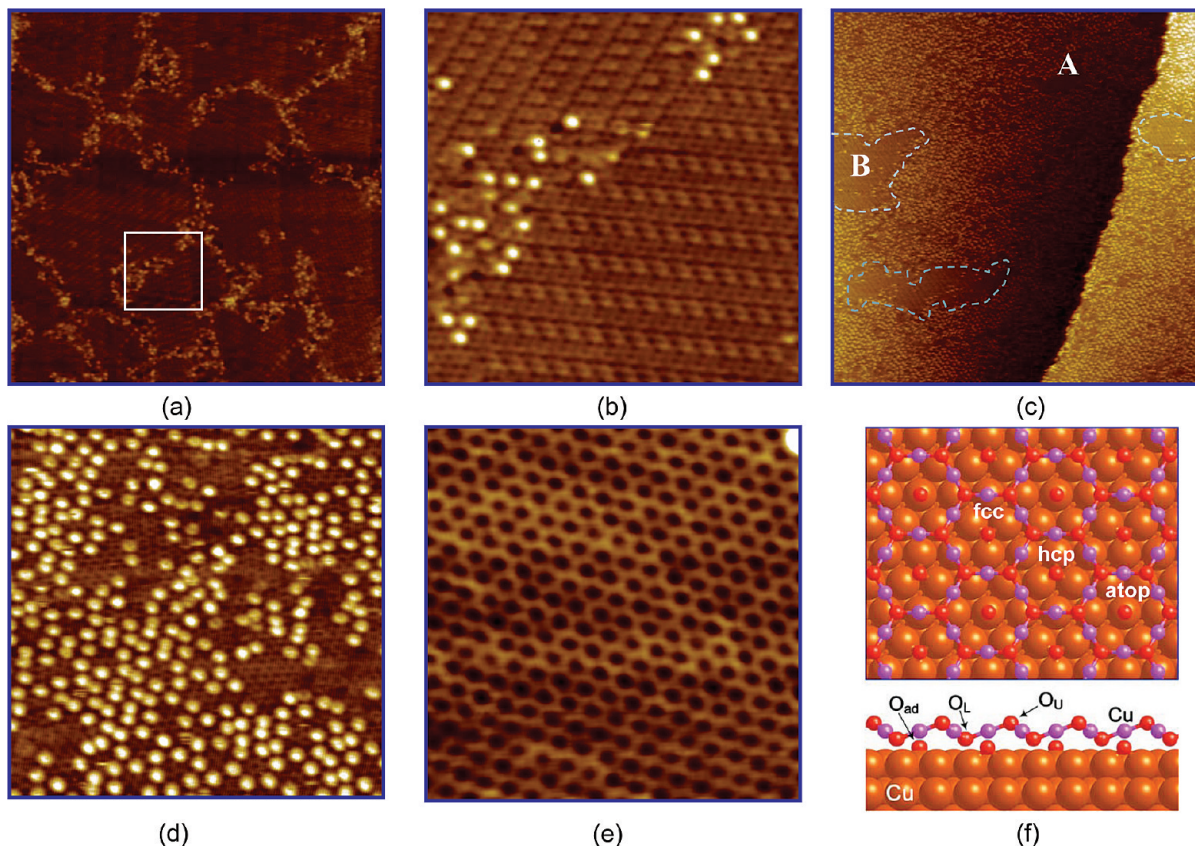


Figure 3. STM images of the Cu₂O surface oxide during the “slow reaction” regime: (a–b) ~ 1000 s and (c–e) ~ 2000 s. Part b is a zoomed-in image of the boxed area in part a. Surface areas of A and B in part c are magnified in d and e, respectively. Image sizes are (a, c) 100×100 nm², (b, d) 20×20 nm², and (e) 8×8 nm². (f) The structural model of e, the Cu₂O(111)-like layer on Cu(111). In the Cu₂O(111)-like layer, Cu atoms are represented by purple balls, and O atoms are represented by red balls. There are three types of adsorption sites for chemisorbed oxygen atoms (fcc, hcp, and atop sites).

phase for later discussion. The decrease in XPS O 1s intensity during the “slow reaction” regime could thus be connected to the appearance and propagation of the “O-deficient Cu₂O” phase.

As surface reduction moves into the “fast reaction” regime, two alternating surface phases emerge on the Cu(111) surface (Figure 4a). The line profile in Figure 4a illustrates the height difference between phases I and II as well as the height difference between two nearest phases I. The height difference between two nearest phases I is around 0.21 nm, which corresponds to the step height of Cu(111) and suggests that neighboring phases of I and II coexist on the same terrace of Cu(111). Phase I, depicted in Figure 4b, has the same structure as the “O-deficient Cu₂O” phase observed in Figure 3d. The structure of phase II is magnified in Figure 4c, featuring bright rings with central depression dispersed randomly on the surface. The bright rings are ~ 1.45 nm in diameter and are interpreted as chemisorbed oxygen atoms dispersed over the Cu(111) surface. The same feature with identical characteristics has been observed by Wiame et al.⁴⁷ during the initial oxidation stage of Cu(111) at room temperature. With the sample bias near the Fermi level, chemisorbed oxygen is regularly observed as depressions on the flat metal surface because the charge transfer depletes the local density of states (LDOS) at the adsorption site.^{49,50} The bright rings surrounding the depressions are caused by the scattering of surface-state electrons on Cu(111).^{47,51,52}

As the reduction reaction proceeds, surface areas of phase II expand at the expense of phase I. Figure 4d displays the surface morphology after ~ 5000 s of CO exposure at 800 K. Phase II has grown wider and occupies $\sim 90\%$ of the total surface area in Figure 4d. After 6000 s of CO exposure at 800 K, phase I

disappears completely, as well as chemisorbed oxygen atoms on phase II. The Cu₂O surface oxide is reduced completely to the metallic Cu phase. The reduction of the Cu₂O surface was studied at several temperatures between 650 and 800 K and in the presence of 10^{-8} – 10^{-6} Torr CO. The kinetic behavior and the intermediate structures observed were always very close to those described in the reduction process above.

Overall, Figures 3 and 4 provide a complete picture for the reduction of a Cu₂O surface in the presence of CO. Instead of a direct conversion from the Cu₂O surface to the metallic Cu phase, we found the reduction reaction goes through two stages: (1) the appearance and propagation of the “O-deficient Cu₂O” phase and (2) the annihilation of the “O-deficient Cu₂O” phase.

II. The Structure of the “O-Deficient Cu₂O” Phase. To enhance our understanding of the reduction kinetics, we now discuss the formation and the structure of the “O-deficient Cu₂O” phase based on DFT calculations and STM studies. In section I, we have shown the “O-deficient Cu₂O” phase originates from the creation of oxygen vacancies in the Cu₂O(111)-like layer. Therefore, DFT calculations were first carried out to look into the atomic and electronic structures of the Cu₂O(111)-like layer on Cu(111). In accordance with the DFT study by Soon et al.,⁴⁶ our calculations also show that there are three types of adsorption sites for chemisorbed oxygen atoms (fcc, hcp, and atop sites, Figure 3f). The fcc hollow site of H_O is more stable than the hcp hollow site by 0.05 eV and the atop site by 0.39 eV. Since the chemisorbed oxygen atom is not stable at the atop site, we considered only chemisorbed oxygen atoms at fcc and hcp sites in the following analysis. To determine the preference of oxygen species to be removed during the CO

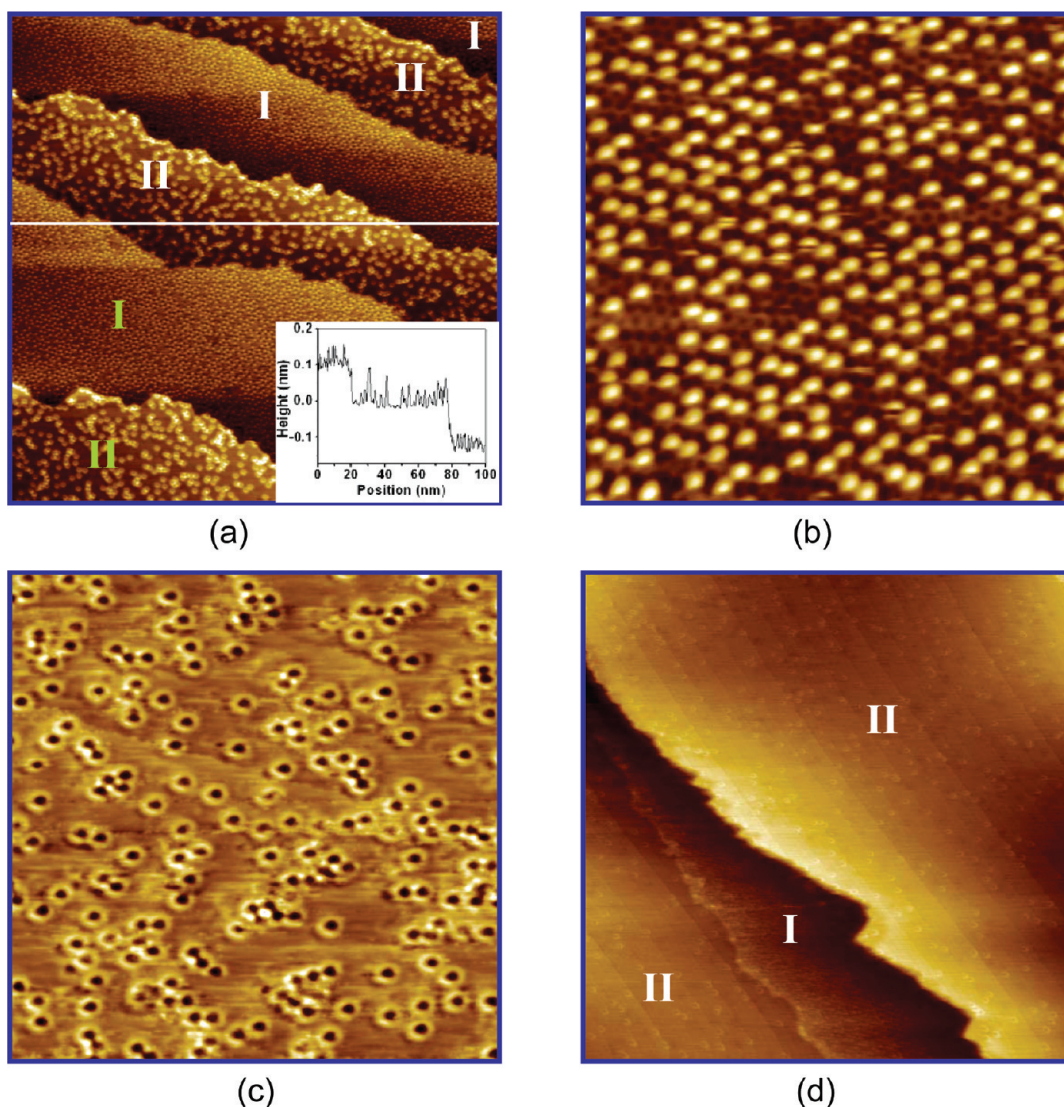


Figure 4. STM images of the Cu_2O surface oxide during the “fast reaction” regime: (a–c) ~ 3500 s and (d) ~ 5000 s. The inset in part a plots the profile across the displayed white line. Two phases appear in the large-scale image of part a and are labeled as I and II. Parts b and c are taken in the areas labeled by green-colored I and II, respectively. Image sizes are (a, d) $100 \times 100 \text{ nm}^2$ and (b, c) $20 \times 20 \text{ nm}^2$.

titration, we estimated ΔE_{R} and ΔG_{R} at 800 K for CO oxidation to CO_2 on the $\text{Cu}_2\text{O}(111)$ -like layer on $\text{Cu}(111)$. ΔG_{R} 's for CO oxidation with all oxygen atoms in the $\text{Cu}_2\text{O}(111)$ -like layer are highly negative, and therefore, the reaction should be energetically favorable at 800 K. The chemisorbed oxygen species ($\text{O}_{\text{ad,hcp}}$ and $\text{O}_{\text{ad,fcc}}$) are the least stable and the most favorable toward CO titration. The corresponding ΔG_{R} 's are indistinguishable (-1.93 versus -1.92 eV). With a less negative $\Delta G_{\text{R}}(-1.82 \text{ eV})$, the next oxygen species to be removed located at the upper oxide layer (O_{U}). This will be followed by the removal of oxygen at lower oxide layer (O_{L} , $\Delta G_{\text{R}} = -1.38 \text{ eV}$). Our DFT predicts that a plausible sequence for CO titration on $\text{Cu}_2\text{O}/\text{Cu}(111)$ is $\text{O}_{\text{ads}} (\text{O}_{\text{ad,hcp}} \sim \text{O}_{\text{ad,fcc}}) < \text{O}_{\text{U}} < \text{O}_{\text{L}}$ with an increasing ΔG_{R} . In agreement with our STM studies, the DFT results also show that CO titration starts with the chemisorbed oxygen.

On the basis of the most stable structure of the $\text{Cu}_2\text{O}(111)$ -like layer, ELF calculations were conducted to investigate the charge redistribution before and after the removal of the chemisorbed oxygen. To simplify the discussion, we denote the Cu_2O honeycomb with/without the chemisorbed oxygen atom as H_0/H_v . As shown in Figure 5a, the removal of chemisorbed oxygen leads to an increasing electron concentra-

tion around Cu atoms in H_v . In addition, the Bader analysis also suggests that the removal of chemisorbed oxygen results in a charge redistribution. The electrons released by the oxygen removal are back-donated to the $\text{Cu}(111)$ substrate and the Cu_2O surface layer. Therefore, the bright-dot feature of the “O-deficient Cu_2O ” phase (Figure 3d and 4b) could be explained by the extra electrons that H_v obtained due to the removal of chemisorbed oxygen at the center. The major component of electronic states at the Fermi level originates from Cu 3d and Cu 4s states in Cu_2O . Upon the removal of chemisorbed oxygen, the extra charge donated back from the removed oxygen flows into the Cu 3d and Cu 4s states and leads to the enhancement of H_v in STM images. In Figures 3d and 4b, the STM tip is only able to resolve H_v as a bright dot at a large tip–surface separation. At a smaller tip–surface separation or upon a change of tip state, the hole of H_v could be resolved (Figure 5b).

The electronic structures of H_0 and H_v could be better visualized through the bias-dependent STM images. The white circle and rectangles in Figure 5c and d mark the same area of the $\text{Cu}_2\text{O}/\text{Cu}(111)$ surface. By comparing the image contrast at the same area, it is obvious that H_v resolved as a bright dot at -1.0 V are resolved as a dark ring at high bias -2.1 V , whereas H_0 resolved as a honeycomb at -1.0 V are resolved as a bright

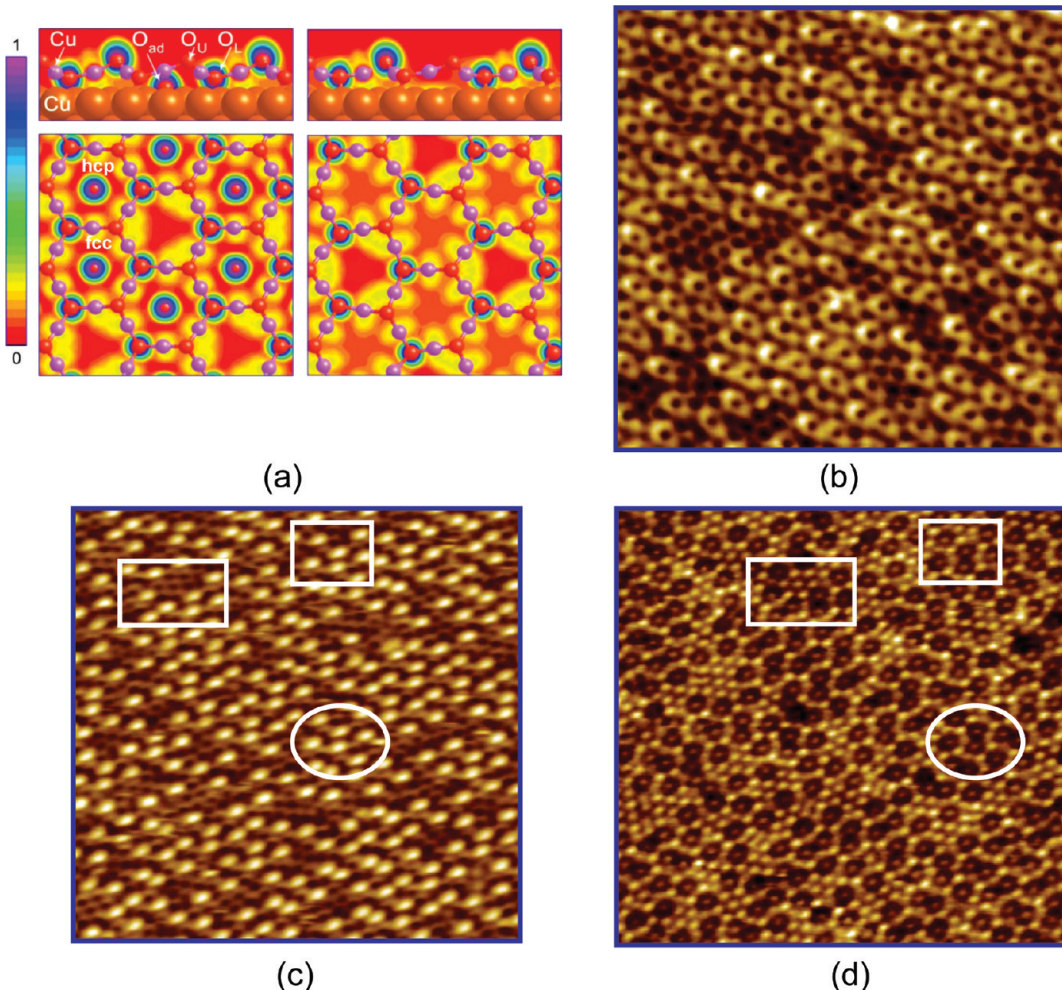


Figure 5. The structure of the “O-deficient Cu₂O” phase. (a) Side and top views of ELF calculations with/without chemisorbed oxygen on Cu₂O/Cu(111). In the Cu₂O surface layer, Cu atoms are represented by purple balls, and O atoms are represented by red balls. (b) STM image of the “O-deficient Cu₂O” phase after a tip change. (c–d) Bias dependent STM images of the “O-deficient Cu₂O” phase. Image sizes and tunneling parameters are (a) $10 \times 10 \text{ nm}^2$, $V_s = -1.0 \text{ V}$, $I = 1.0 \text{ nA}$; (c) $20 \times 20 \text{ nm}^2$, $V_s = -1.0 \text{ V}$, $I = 0.1 \text{ nA}$; and (d) $20 \times 20 \text{ nm}^2$, $V_s = -2.1 \text{ V}$, $I = 0.1 \text{ nA}$. The same surface areas are marked by white squares and circles.

spot at high bias -2.1 V . The reversed contrast suggests the STM tip is probing states of different species at these two biases. At the sample bias of -1.0 V , the component of Cu 3d and Cu 4s states dominates the LDOS. At the sample bias of -2.1 V , the tip is tunneling into the resonance of chemisorbed oxygen at the surface. H_O is thus highlighted as a bright spot, whereas H_V is resolved as a dark ring. The bright spot at the center of H_V originates from the contribution of Cu 3d states from the copper substrate.

In fact, the removal of chemisorbed oxygen not only leads to the change of electronic structure in the Cu₂O layer, but also causes the Cu₂O layer to reconstruct geometrically. It is evident from Figure 5 that the formation of H_V leads to the distortion and compression of neighboring H_O. H_O distant from H_V is not distorted and retains a periodicity of 0.60 nm . The expansion of H_V is caused by the strain released at the H_V site, since there is a lattice mismatch of 18% between the Cu₂O(111)-like layer and the Cu(111) substrate. Close inspection of STM images of the “O-deficient Cu₂O” phase finds that the distribution of H_V could be categorized into two main configurations: isolated H_V units and H_V pairs. As shown in Figure 6a and 6b, the solid ellipses mark two H_V's that are separated from each other by surrounding H_O's. The dotted ellipses mark a pair of H_V's that are sitting next to each other. Due to the expansion of H_V, each isolated H_V is surrounded by 7 H_O, and each H_V pair is

surrounded by 10 H_O. Clearly, the formation of oxygen vacancy causes the reconstruction of the Cu₂O honeycomb into a heptagon. The distortion of H_V after the removal of chemisorbed oxygen was also observed in our DFT calculations (Figure 5a), although the experimentally observed reconstruction of H_V into a heptagon cannot be captured by the DFT calculations due to the limited size of the supercell.

The structural configurations of H_O and H_V are illustrated in Figure 6c and d. Figure 6c is an inverted image of Figure 6b and shows an enhanced contrast for the Cu₂O network. The structural diagram of Figure 6b is also superimposed in Figure 6c and displayed in color as Figure 6d. Figure 6c and 6d demonstrate that all H_V's have a heptagon structure, whereas H_Os can be either hexagonal or pentagonal. The expanded H_V heptagon lowers the local density of Cu₂O, which is compensated via shrinking of H_O's surrounding H_V and the formation of H_O pentagon. Overall, the surface density of Cu₂O is conserved during the formation of the “O-deficient Cu₂O” phase.

Notice that if we assume the bond length between O and Cu in H_V is the same as that in nondistorted hexagonal H_O, the surface area of H_V is 1.4 times larger than nondistorted H_O. From Figure 6b, the surface area of H_V is estimated to be $\sim 1.4\text{--}2.0$ times larger than nondistorted H_O, suggesting an increased bond length and thus the decreased bond strength between O and Cu in H_V.

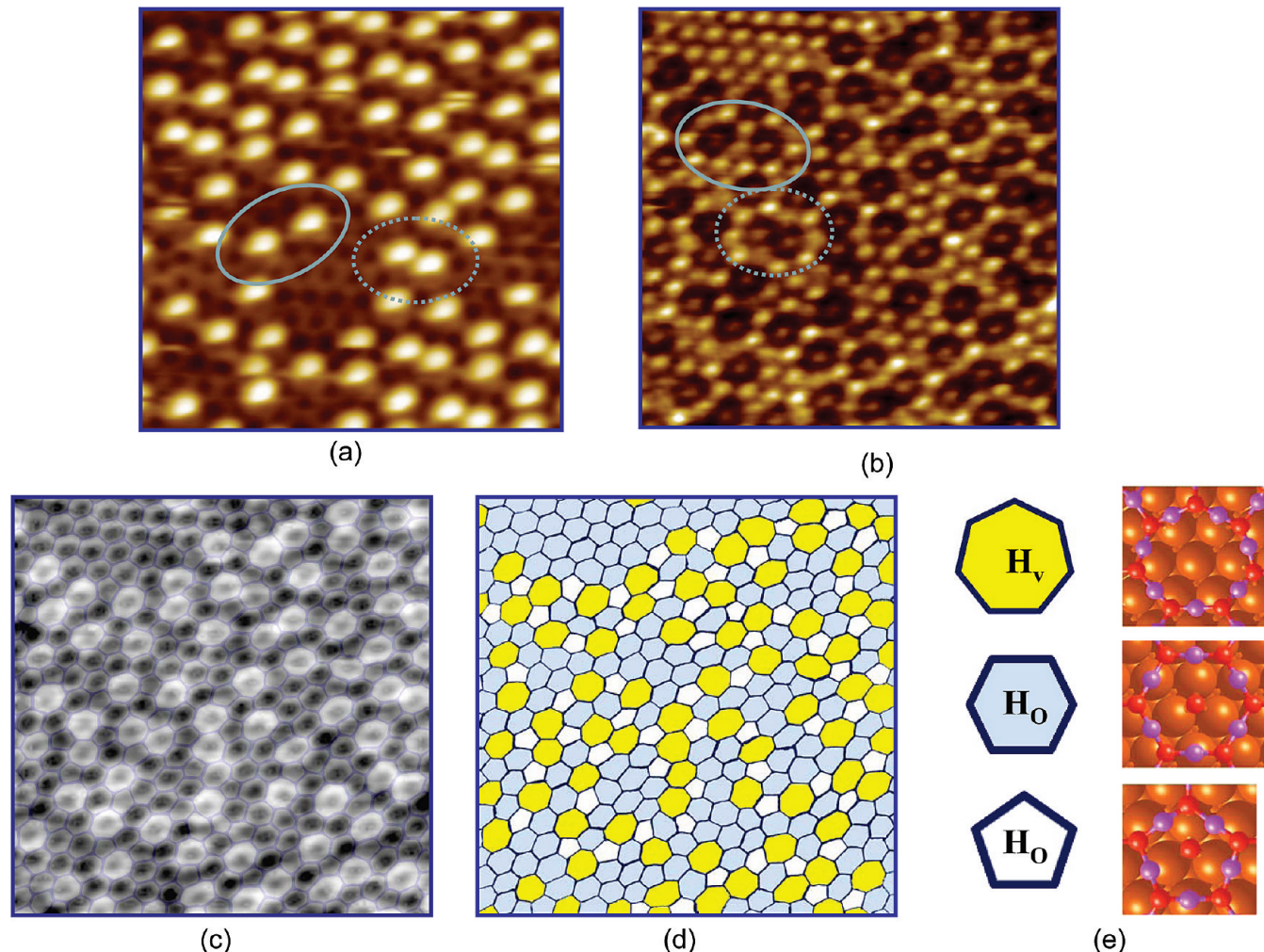


Figure 6. The structural configuration and spacial distribution of H_v and H_o . (a–b) Zoomed-in STM images ($10 \times 10 \text{ nm}^2$) of the “O-deficient Cu_2O ” phase, featuring H_v units surrounded by H_o units. H_v ’s are reconstructed into heptagons. Solid and dotted ellipses mark the two configurations of H_v , isolated H_v and H_v pairs. (c) The inverted STM image of part b with a structural diagram superimposed. (d) The structural diagram of part b. H_v ’s are painted in yellow, H_o ’s are painted in blue and white. (e) Schematic illustrations of the structural configurations of H_v and H_o . Cu atoms in Cu_2O are represented by purple balls, and O atoms are represented by red balls. Cu atoms in the $\text{Cu}(111)$ substrate are represented by orange balls.

III. The Pathway for the Reduction of the Cu_2O Surface Layer.

At the initial stage of surface reduction, the creation of H_v in the close-packed “44” Cu_2O surface oxide might go through a direct reaction between surface oxygen and gas phase CO. The reaction probability is low, and thus, we observed an induction period ($\sim 1200 \text{ s}$) in Figure 2. Upon the formation of an H_v , the strain of the Cu_2O surface oxide is released at H_v , which leads to the relaxation of the ordered “44” surface oxide and induces the formation of domain boundaries. Multiple H_v sites at the surface cause the meandering of domain boundaries, which breaks a large terrace into many small domains.

The formation of H_v also provides an adsorption site for CO. Meanwhile, the distortion of neighboring H_o leads to a closer distance between chemisorbed oxygen and surrounding lattice oxygen in H_o . Activated by the repulsive interaction from the surrounding lattice oxygen in Cu_2O , chemisorbed oxygen then hops to H_v and reacts with adsorbed CO there. The formed CO_2 leaves the surface and creates a neighboring H_v pair, which provides sites for the subsequent interaction with CO and further removal of chemisorbed oxygen at neighboring H_o . As a result, the removal of chemisorbed oxygen and the propagation of H_v accelerate across the surface, which explains the decay in XPS O 1s intensity during the “slow reaction” regime. Since the

domain boundaries are enriched with distorted H_o , the propagation of H_v starts along the domain boundaries. The discontinuous distribution of H_v in Figure 6 suggests that H_v diffuses across the surface via the hopping of chemisorbed oxygen atoms between neighboring H_o and H_v units. The diffusion of H_v units facilitates the propagation of the “O-deficient Cu_2O ” phase.

As the “O-deficient Cu_2O ” phase propagates across the surface, the annihilation of the “O-deficient Cu_2O ” phase starts, and the reduction of the Cu_2O surface oxide enters into the “fast reaction” regime. The annihilation of the “O-deficient Cu_2O ” phase starts from step edge sites, which is unambiguously evidenced by the appearance of alternating $\text{Cu}_2\text{O}/\text{Cu}$ phases (phases I/II). Considering the broken symmetry and lower coordination of oxygen, lattice oxygen within H_v at step edge sites is the least stable and most likely to be removed by CO. During the annihilation of the “O-deficient Cu_2O ” phase, H_v is enriched at step edges, as illustrated by the enhanced number of dots at step edges in Figure 4. The enrichment of H_v at step edges could be explained by chemisorbed oxygen atoms diffusing from H_o ’s at edge sites to the metallic Cu surface and reacting with adsorbed CO there.

Upon the removal of lattice oxygen from the “O-deficient Cu_2O ” phase, Cu is released to the terrace while the underneath

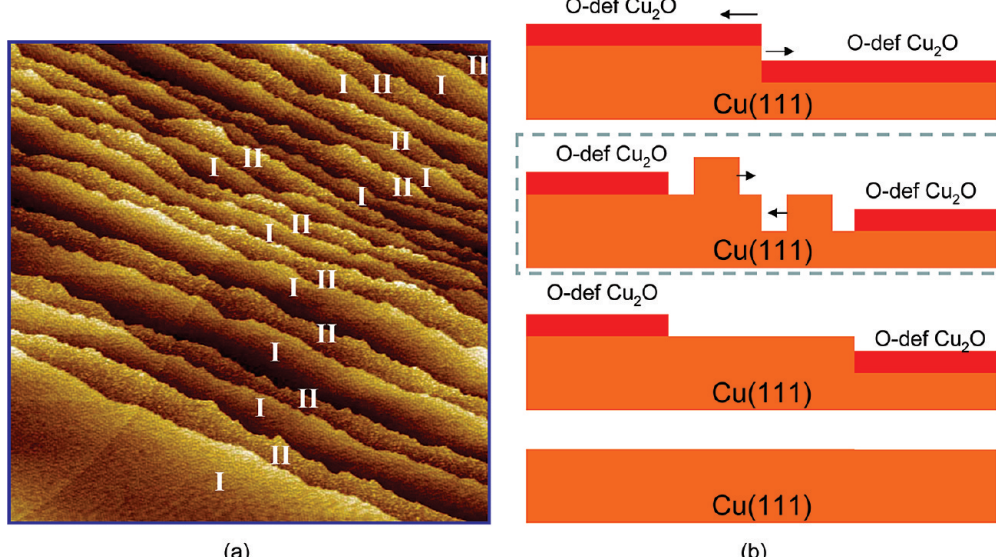


Figure 7. (a) Large scale STM image ($500 \times 500 \text{ nm}^2$) of the Cu₂O surface oxide during the “fast reaction” regime. I and II represent the alternating phases of “O-deficient Cu₂O” and “metallic Cu”. (b) Schematic illustration on the annihilation of the “O-deficient Cu₂O” phase. “O-def” is the abbreviation for “O-deficient”.

metallic Cu phase is exposed. The removal rate of Cu₂O could be measured through the formation and development of the metallic Cu phase. Figure 7a shows the metallic Cu phase developed at each terrace has a comparable width along the direction perpendicular to the step orientation, whereas the width of terraces covered by Cu₂O varies from 10 to 100 nm. The similar terrace width of the metallic Cu phase suggests a similar removal rate of Cu₂O at each terrace. Note that there are no preferred step sites or preference of step orientation observed in the removal of Cu₂O. The removal of Cu₂O is approximately linear to the length of steps, which explains the constant reaction rate measured during the “fast reaction” regime. Prior to the complete reduction of Cu₂O surface oxide, the length of steps decreases, and subsequently, the reduction rate drops.

The development of the metallic Cu phase involves surface diffusion of Cu atoms released from the Cu₂O lattice and is illustrated in Figure 7b. Here, we assume the removal of Cu₂O starts along both directions against the step, up-step and down-step. Since the area density of Cu in Cu(111) is 1.86 times higher than that of the Cu₂O(111)-like layer, Cu atoms released from the Cu₂O surface oxide would occupy only about half of the surface area Cu₂O takes. (The area density of Cu is given by $2x/(\sqrt{3}a^2)$, where x is the number of Cu atoms in each unit cell and a is the unit cell length.) This is illustrated in the dashed-box scheme of Figure 7b, which assumes the released Cu atoms have limited diffusivity and form islands on the Cu(111) surface. However, adislands of Cu are not observed throughout the reduction of Cu₂O surface oxide. At 800 K, Cu adatoms released from the Cu₂O lattice have enough diffusivity to reach and attach to the nearby steps. Giesen et al. have illustrated that Cu islands decay rapidly on Cu(111), via both Ostwald ripening and island migration, at 318 K and above.⁵³ Therefore, the development of metallic Cu phase is limited only by the rate of CO reaction with lattice oxygen at step edges.

Note that Cu atoms released at the upper terrace could attach only to the lower step because the diffusion path to the upper step is blocked by the Cu₂O surface oxide, which has a much larger Schwoebel barrier and surface diffusion barrier. The diffusion of Cu atoms to the lower terrace leads to the formation of alternating phases observed in Figure 4a. The removal rate of Cu₂O at both up-step and down-step directions could also

be compared since the diffusion of Cu atoms is limited between the Cu₂O surface oxide at the upper terrace and at the lower terrace. Assuming the removal rate at the up-step direction is v_U and the removal rate at the down-step direction is v_L , the surface area occupied by Cu atoms released from Cu₂O, $(v_U + v_L)t/1.86$, should be equal to surface area created by removing Cu₂O at the lower terrace, v_{Lt} . Hence, the removal rate at the down-step direction, v_L , is 1.16 times higher than the removal rate at the up-step direction, v_U . The higher removal rate at down-step direction suggests the reduction at the lower-terrace side of Cu₂O is accelerated by Cu adatoms diffused from the upper terrace.

The propagation of reaction front for CO titration on the Cu₂O surface oxide exhibits patterns distinct from the CO titration experiments on metal surfaces covered with chemisorbed oxygen.²³ The reaction front propagates uniformly along the phase boundaries at steps and forms the “alternating-stripe” pattern, as opposed to the “island-growth” pattern regularly observed in CO titration of chemisorbed oxygen on the metal surfaces. The distinct pattern in the reduction of Cu₂O surface oxide illustrates the limited reactivity of lattice oxygen in the Cu₂O surface oxide, in contrast with the more active chemisorbed oxygen adsorbed on the Cu substrate.

Summary and Conclusions

In summary, the existence of an induction time and an autocatalytic reaction for the reduction of Cu₂O/Cu(111) surfaces by CO was demonstrated through a combined STM, XPS, and DFT study. Real-time XPS measurements show that the reduction kinetics of a Cu₂O surface layer can be divided in two stages: the “slow reaction” regime and the “fast reaction” regime. Both the STM and DFT studies show that during the “slow reaction” regime, CO reacts only with chemisorbed oxygen atoms within the Cu₂O surface oxide. The slow removal rate could be explained by the low sticking coefficient of CO on a well-ordered Cu₂O surface layer.

Upon the creation of oxygen vacancies, the ordered Cu₂O surface oxide is developed into an “O-deficient Cu₂O” phase. The “O-deficient Cu₂O” phase is a disordered phase linked to the formation of Cu₂O heptagons. A Cu₂O heptagon originates

from the reconstruction of a Cu₂O honeycomb upon the loss of the chemisorbed oxygen at the center. The Cu₂O heptagon causes the contraction of neighboring Cu₂O honeycombs and facilitates the diffusion of chemisorbed oxygen in these honeycombs. The Cu₂O heptagon also provides an adsorption site for CO, which reacts with chemisorbed oxygen hopped from neighboring Cu₂O honeycombs. As a result, the creation of oxygen vacancies and the propagation of the “O-deficient Cu₂O” phase accelerate across the surface. The spacial distribution of Cu₂O heptagons suggests that the propagation of the “O-deficient Cu₂O” phase is facilitated by the diffusion of chemisorbed oxygen atoms between neighboring Cu₂O honeycombs and Cu₂O heptagons.

The formation of a Cu₂O heptagon lowers the reaction barrier for the removal of lattice oxygen from Cu₂O. The propagation of Cu₂O heptagons leads to the “fast reaction” regime, where CO reacts only with Cu₂O heptagons at step edges. The uniform reaction rate at step edges explains the linear decrease of surface oxygen coverage during the “fast reaction” regime. The reduction of Cu₂O also leads to a release of Cu atoms from Cu₂O. The propagation of the metallic Cu phase could be used to measure the removal rate of Cu₂O, which shows the reduction of Cu₂O oxide at a lower terrace is accelerated by Cu atoms diffused from an upper terrace.

Through the formation and propagation of the “O-deficient Cu₂O” phase, CO reduction of a Cu₂O surface oxide supported on Cu(111) exhibits an autocatalytic kinetics. The observed intermediate structures and reaction pathway provide an insight to understand the reduction chemistry on copper oxides as well as the reactivity of surface oxides of late transition metals.

Acknowledgment. The authors are thankful to the U.S. Department of Energy (Chemical Sciences Division, DE-AC02-98CH10886 and DE-AC02-05CH11231 Grants) for financial support. DFT calculations were carried out at Center for Functional Nanomaterials at Brookhaven National Laboratory and National Energy Research Scientific Computing (NERSC) Center.

References and Notes

- (1) Szanyi, J.; Goodman, D. W. *Catal. Lett.* **1992**, *14*, 27–35.
- (2) Szanyi, J.; Goodman, D. W. *Catal. Lett.* **1993**, *21*, 165–174.
- (3) (a) Szanyi, J.; Goodman, D. W. *Stud. Surf. Sci. Catal.* **1993**, *75*, 1599–1602. (b) Domagala, M. E.; Campbell, C. T. *Catal. Lett.* **1991**, *9*, 65–70.
- (4) Klier, K.; Eley, H. P.; Paul, B. W. *Adv. Catal.* **1982**, *31*, 243–313.
- (5) Newsome, D. S. *Catal. Rev. Sci. Eng.* **1980**, *21*, 275–318.
- (6) O’Keeffe, M.; Bovin, J. O. *Am. Mineral.* **1978**, *63*, 180–185.
- (7) JCPDS Powder Diffraction File; Int. Center For Diffraction Data: Swarthmore, PA, 1989; PDFs #41-0254, 05-0667, and 083-1665.
- (8) Henrich, V. E.; Cox, P. A. *The Surface Science of Metal Oxides*; Cambridge University Press: Cambridge, U.K., 1994.
- (9) Rodriguez, J. A.; Hanson, J. C.; Frenkel, A. I.; Kim, J. Y.; Pérez, M. *J. Am. Chem. Soc.* **2002**, *124*, 346–354.
- (10) (a) Wang, X. Q.; Hanson, J. C.; Frenkel, A. I.; Kim, J. Y.; Rodriguez, J. A. *J. Phys. Chem. B* **2004**, *108*, 13667–13673. (b) Kim, J. Y.; Rodriguez, J. A.; Hanson, J. C.; Frenkel, A. I.; Lee, P. L. *J. Am. Chem. Soc.* **2003**, *125*, 10684–10692. (c) Rodriguez, J. A.; Kim, J. Y.; Hanson, J. C.; Perez, M.; Frenkel, A. I. *Catal. Lett.* **2003**, *85*, 247–254.
- (11) (a) Over, H.; Kim, Y. D.; Seitsonen, A. P.; Wendt, S.; Lundgren, E.; Schmid, M.; Varga, P.; Morgante, A.; Ertl, G. *Science* **2000**, *287*, 1474–1476. (b) Lundgren, E.; Gustafson, J.; Resta, A.; Weissenrieder, J.; Mikkelsen, A.; Andersen, J. N.; Kohler, L.; Kresse, G.; Klikovits, J.; Biederman, A.; Schmid, M.; Varga, P. *J. Electron Spectrosc. Relat. Phenom.* **2005**, *144*, 367–372. (c) Klikovits, J.; Schmid, M.; Gustafson, J.; Mikkelsen, A.; Resta, A.; Lundgren, E.; Andersen, J. N.; Varga, P. *J. Phys. Chem. B* **2006**, *110*, 9966–9975.
- (12) (a) McClure, S. M.; Lundwall, M.; Yang, F.; Zhou, Z.; Goodman, D. W. *J. Phys. Chem. C* **2009**, *113*, 9688–9697. (b) McClure, S. M.; Goodman, D. W. *Chem. Phys. Lett.* **2009**, *469*, 1–13.
- (13) (a) Kim, S. H.; Wintterlin, J. *J. Phys. Chem. B* **2004**, *108*, 14565–14569. (b) Kim, Y. K.; Zhang, Z. R.; Parkinson, G. S.; Li, S. C.; Kay, B. D.; Dohnalek, Z. *J. Phys. Chem. C* **2009**, *113*, 20020–20028.
- (14) (a) Gao, F.; Wang, Y.; Cai, Y.; Goodman, D. W. *J. Phys. Chem. C* **2009**, *113*, 174–181. (b) Gao, F.; Cai, Y.; Gath, K. K.; Wang, Y.; Chen, M. S.; Guo, Q. L.; Goodman, D. W. *J. Phys. Chem. C* **2009**, *113*, 182–192.
- (15) (a) Knudsen, J.; Merte, L. R.; Grabow, L. C.; Eichhorn, F. M.; Porsgaard, S.; Zeuthen, H.; Vang, R. T.; Laegsgaard, E.; Mavrikakis, M.; Besenbacher, F. *Surf. Sci.* **2010**, *604*, 11–20. (b) Dudin, P.; Barinov, A.; Gregoratti, L.; Kiskinova, M.; Esch, F.; Dri, C.; Africh, C.; Comelli, G. *J. Phys. Chem. B* **2005**, *109*, 13649–13655.
- (16) Over, H.; Balmes, O.; Lundgren, E. *Catal. Today* **2009**, *145*, 236–242.
- (17) Hendriksen, B. L. M.; Bobaru, S. C.; Frenken, J. W. M. *Top. Catal.* **2005**, *36*, 43–54.
- (18) Stampfl, C.; Soon, A.; Piccinin, S.; Shi, H. Q.; Zhang, H. *J. Phys.: Condens. Matter* **2008**, *20*, 184021–19.
- (19) Chen, M. S.; Cal, Y.; Yan, Z.; Gath, K. K.; Axnanda, S.; Goodman, D. W. *Surf. Sci.* **2007**, *601*, 5326–5331.
- (20) Flege, J. I.; Suttor, P. *Phys. Rev. B* **2008**, *78*, 153402–3.
- (21) Flege, J. I.; Hrbek, J.; Suttor, P. *Phys. Rev. B* **2008**, *78*, 165407–5.
- (22) Ackermann, M. D.; Pedersen, T. M.; Hendriksen, B. L. M.; Robach, O.; Bobaru, S. C.; Popa, I.; Quiros, C.; Kim, H.; Hammer, B.; Ferrer, S.; Frenken, J. W. M. *Phys. Rev. Lett.* **2005**, *95*, 255505–4.
- (23) Wintterlin, J. *Adv. Catal.* **2000**, *45*, 131–206.
- (24) Kim, S. H.; Mendez, J.; Wintterlin, J.; Ertl, G. *Phys. Rev. B* **2005**, *72*, 155414–5.
- (25) Leibsle, F. M.; Murray, P. W.; Francis, S. M.; Thornton, G.; Bowker, M. *Nature* **1993**, *363*, 706–709.
- (26) Klust, A.; Madix, R. J. *J. Chem. Phys.* **2007**, *126*, 084707–6.
- (27) Nakagoe, O.; Watanabe, K.; Takagi, N.; Matsumoto, Y. *Phys. Rev. Lett.* **2003**, *90*, 226105–4.
- (28) Schoiswohl, J.; Surnev, S.; Netzer, F. P. *Top. Catal.* **2005**, *36*, 91–105.
- (29) Hartmann, N.; Madix, R. J. *Surf. Sci.* **2002**, *516*, 230–236.
- (30) Kresse, G.; Hafner, J. *Phys. Rev. B* **1993**, *47*, 558–561.
- (31) Kresse, G.; Furthmüller, J. *Phys. Rev. B* **1996**, *54*, 11169–11186.
- (32) Blöchl, P. E. *Phys. Rev. B* **1994**, *50*, 17953–17979.
- (33) Perdew, J. P.; Wang, Y. *Phys. Rev. B* **1992**, *45*, 13244.
- (34) Monkhorst, H. J.; Pack, J. D. *Phys. Rev. B* **1976**, *13*, 5188–5192.
- (35) *CRC Handbook of Chemistry and Physics*; CRC Press: New York, 2002.
- (36) Rodriguez, J. A.; Liu, P.; Vines, F.; Illas, F.; Takahashi, Y.; Nakamura, K. *Angew. Chem., Int. Ed.* **2008**, *47*, 6685–6689.
- (37) Becke, A. D.; Edgecombe, K. E. *J. Chem. Phys.* **1990**, *92*, 5357–5403.
- (38) Savin, A.; Jepsen, O.; Flad, J.; Andersen, O. K.; Preuss, H.; von Schnering, H. G. *Angew. Chem., Int. Ed.* **1992**, *31*, 187–188.
- (39) Henkelman, G.; Arnaldsson, A.; Jónsson, H. *Comput. Mater. Sci.* **2006**, *36*, 354–360.
- (40) Bader, R. F. W.; Beddall, P. M. *J. Chem. Phys.* **1972**, *56*, 3320–3329.
- (41) Bader, R. F. W. *Atoms in Molecules: A Quantum Theory*; Clarendon Press: Oxford, 1994.
- (42) Laidler, K. J. *Chemical Kinetics*, 3rd ed.; Harper and Row: New York, 1987.
- (43) Matsumoto, T.; Bennett, R. A.; Stone, P.; Yamada, T.; Domen, K.; Bowker, M. *Surf. Sci.* **2001**, *471*, 225–245.
- (44) Jensen, F.; Besenbacher, F.; Laegsgaard, E.; Stensgaard, I. *Surf. Sci.* **1991**, *259*, L774–L780.
- (45) Jensen, F.; Besenbacher, F.; Stensgaard, I. *Surf. Sci.* **1992**, *270*, 400–404.
- (46) Soon, A.; Todorova, M.; Delley, B.; Stampfl, C. *Phys. Rev. B* **2006**, *73*, 165424–12.
- (47) Wiame, F.; Maurice, V.; Marcus, P. *Surf. Sci.* **2007**, *601*, 1193–1204.
- (48) Onsten, A.; Gothelid, M.; Karlsson, U. O. *Surf. Sci.* **2009**, *603*, 257–264.
- (49) Besenbacher, F.; Norskov, J. K. *Prog. Surf. Sci.* **1993**, *44*, 5–66.
- (50) Calleja, F.; Arnaud, A.; Hinarejos, J. J.; Vázquez de Parga, A. L.; Hofer, W. A.; Echenique, P. M.; Miranda, R. *Phys. Rev. Lett.* **2004**, *92*, 206101–4.
- (51) Petersen, L.; Laitenberger, P.; Laegsgaard, E.; Besenbacher, F. *Phys. Rev. B* **1998**, *58*, 7361–7366.
- (52) Friedel, J. *Il Nuovo Cimento* **1958**, *7*, 287–311.
- (53) Giesen, M.; Schulze Icking-Konert, G.; Ibach, H. *Phys. Rev. Lett.* **1998**, *80*, 552–555.